Chapter 4

Hα and [OIII] Spectroscopic Insight From High-Redshift Ultra-Luminous Infrared Sources

SMGs are inferred to have high star-formation rates, SFR $\sim 100 - 1000$ $M_\odot$ yr^{-1} and large stellar masses, $M_{stellar} \gtrsim 10^{11}$ $M_\odot$. These findings suggest that SMGs are undergoing intense starburst episodes and that they may be major sites of stellar build up. As part of a continuing program to understand these sources and their context, we sought rest-frame optical line emission from a sample of submm- and mm-detected galaxies at a mean redshift, $< z > \sim 2.0$, with the Near-Infrared Spectrograph (NIRSPEC) on the Keck Telescope to identify the presence of AGN in the center of these galaxies through detection of broad Hα and [OIII] lines, and using the line ratio diagnostics from [NII]/Hα and [SII]/Hα. Our results emphasize the challenges faced by long-slit spectroscopic techniques when both AGN and star-forming activity are present: we demonstrate that rest-frame optical emission line-widths may be enhanced by emission from the broad-line region near a central AGN and thus result in overestimates of dynamical masses.

4.1 Introduction

Ultra-luminous infrared galaxies (ULIRGs; $L_{8-1000\ \mu m} > 10^{12}$ $L_\odot$) contribute a negligible fraction of local star formation, but are major sites of massive star formation

Table 4.1. Summary of *NIRSPEC* Observations

Name	RA[a] ($h\,m\,s$)	Dec. ($^\circ\,'\,''$)	NIRSPEC Filter	Exposure times ks	Date
SMM J030227.73	03:02:27.73	+00:06:53.5	N5	3.0	Aug. 2004
SMM J123716.01	12:37:16.01	+62:03:23.3	N6	1.8	April 2006
SMM J123549.44	12:35:49.44	+62:15:36.8	N7	7.2	April 2006
			[OIII] (N5)	7.2	April 2006
SMM J123635.59	12:36:35.59	+62:14:24.1	N4	9.0	April 2006
MIPS 142824.0	14:28:24.0	+35:26:19	N7	2.4	March 2005

[a] Radio center from C05 compilation

and metal production at higher redshifts, where they have been identified only by the detection of their thermal dust emission in the millimeter (mm) and sub-mm wavebands (Smail et al. 1997; Barger, Cowie & Sanders 1999; Eales et al. 1999; Bertoldi et al. 2000; Cowie et al. 2002; Scott et al. 2002; Borys et al. 2003; Webb et al. 2003b; Coppin et al. 2005; Younger et al. 2007). Furthermore, the space density of these extreme galaxies appears to increase by a factor of ~ 1000 from $z \sim 0$ to $z \sim 2$ (C05; Le Floc'h et al. 2005; Caputi et al. 2007).

Rest-frame UV redshifts have been extremely valuable to understand the luminosity, astrophysical nature and to enable follow-up observations of SMGs. They have revealed that the redshift distribution of radio-identified SMGs coincides with the epoch of peak quasar activity, with a significant contribution to the global SFR density at $z = 2 - 3$ not traced in the UV (C05). However, UV lines are typically subject to offsets from galactic outflows and winds: velocity offsets of up to $few \times 1000$ km s^{-1} have been found in SMGs between Lyα, Hα and molecular CO lines (Greve et al. 2005; Swinbank et al. 2004, hereafter S04; Takata et al. 2006). Even though these offsets provide information about the winds in SMGs and their effect on the surrounding inter-galactic medium (Heckman 2001), they can also confuse the accurate identification of groups of galaxies associated with the same large-scale structures (Blain et al. 2002). Furthermore, these offsets can be sufficiently large to fail to deliver the necessary redshift accuracy needed to undertake some detailed follow-up observations. For example, observations of CO emission have traditionally

required high precision, due to the narrow observed mm-wave frequency band. It is thus important to obtain more accurate redshifts for the interstellar medium in the SMGs. Rest-frame optical lines should provide a more accurate redshift for the bulk of the gas in the interstellar medium of the potential well of the galaxy. Further, at $z \sim 2$ the near-IR traces a rich array of rest-frame optical emission lines, including the Balmer lines (e.g., Hα, Hβ) and a number of forbidden lines (e.g., [NII], [SII], [OIII]) that enable us to probe their astrophysics.

Low-resolution near-IR observations can resolve the ratio of the adjacent [NII] and Hα line strengths, the so-called N2-index, which has been shown to correlate well with the (12+log[O/H]) metallicity indicator. The [NII] line traces diffuse ionized medium and, together with Hα, it is sensitive to the hardness of the radiation. Together with the [SII]/Hα line ratio, the N2-index can be used as a coarse metallicity estimate and can indicate the presence of an AGN radiation field if [NII] and/or [SII] are very strong (e.g., Veilleux et al. 1995).

S04 reported a large program of near-IR follow up observations of 30 radio-identified SMGs from the C05 sample, using long-slit Hα observations with the Near-Infrared Spectrograph (NIRSPEC; McLean et al. 1998) instrument at Keck. We present here a continuation of this program, including observations of multiple lines in four radio-identified submm-detected galaxies from C05 and the mm-detected galaxy, MIPS 142824.0 (Borys et al. 2006). We present our sample and observing strategy in §4.2 and describe our reduction and analysis in §4.3. Our results are shown in §4.4 and discussed in detail in §4.5.

4.2 Sample Selection and Observing Strategy

Four out of the five sources presented here were drawn from the sample of radio-identified SMGs in C05. Based on rest-frame UV observations with the blue-sensitive Low-Resolution Imaging Spectrograph on Keck (LRIS-B; Oke et al. 1995; McCarthy et al. 1998), C05 spectroscopically-confirmed these objects to be in the redshift range $1.4 \lesssim z \lesssim 2.2$. We make no target selection based on UV properties, and thus

maintain diverse UV properties within our sample.

We also include in our sample a hyper-luminous galaxy ($L_{8-1000\ \mu m} \gtrsim 10^{13}\ L_{\odot}$) detected in all three bands of the Multiband Imager for *Spitzer* (MIPS: $24, 70, 160\ \mu$m; Rieke et al. 2004). With no evident AGN signatures at wavelengths ranging from the optical to the radio, this galaxy has been interpreted as powered entirely by star formation and thus a likely analog to the SMGs that are found at higher redshifts (see Borys et al. 2006).

Our selection criteria also include observing feasibility. Our targets are too faint to be detected in short exposures, making it necessary to use nearby bright stars as references for blind telescope pointing offsets, based on deep K-band imaging (e.g., Smail et al. 2004). Therefore, we select objects that have a near-IR bright star within $1'$. We also selected our targets to have both Hα and [OIII] lines redshifted into regions of the near-IR atmospheric windows that are relatively free of sky line emission.

Our science observations consist on repeating a series of ABBA sequences, each sequence comprising 4×15-min frames (each frame usually built from three coadds of 300s each) with the science target at two different positions on the NIRSPEC slit, separated by $\sim 15 - 20''$. For flux-calibration purposes, we perform a short exposure of a Vega-type ($A0$) standard star, with weak stellar absorption features, using the exact instrument setup for each science target. Furthermore, we take repeated frames of the standard star at different positions along the slit with spacings of $\sim 15''$ for rectification purposes.

For the redshifts covered by our sample, Balmer and [OIII] emission lines are redshifted into the H- and K-band. We used the low-resolution setting of NIRSPEC with the $42'' \times 0.76''$ slit, achieving a resolution of $R \sim 2000$ (see Section 4.3). We collected our data from August 2004 to April 2006. Observing conditions were of varying quality, with occasional clouds and seeing $\sim 0.8 - 1.5''$ in the V-band. Details of our observations are summarized in Table 4.1.

4.3 Reduction and Analysis

We reduced the spectra using the IRAF package. Preliminary reduction steps comprise elimination of bad pixels using the combined dark frames and removal of cosmic rays. Spatial correction is required to place the wavelength direction along the y-axis and the spatial direction along the x-axis. We do a rough spatial rectification of the spectrum by applying a rotation of 5.1 degrees, followed by a curvature correction defined by the trace of the standard star. We base our wavelength solution on the identification of Argon lines from calibration lamps, using the IRAF tasks IDENTIFY and REIDENTIFY.

We rely on nod-subtraction within each ABBA sequence for the bulk of sky subtraction. We create two (A - B) pairs from each ABBA sequence. Each of these nod-subtracted images display a positive and a negative trace of the science targets. We reduce persistent OH-line emission in these 2D spectra by fitting a polynomial along the spatial direction and subtracting it with IRAF's BACKGROUND task. We show the 2D spectra of our targets in the top panels of Figs. 4.1-4.5. We define our instrumental spectral resolution by measuring the width of individual OH lines ($\sim$ 10 Å). In the K-band this translates to an achieved resolution of $R \sim 2000$. We use the measured width of sky lines to correct for instrument resolution in determining the FWHM of the emission lines. We apply this correction by adding the science emission line FWHM and the sky-line width in quadrature, $\mathrm{FWHM}_{corr} = \sqrt{(FWHM_{obs})^2 - (10\ \text{Å})^2}$, where typically $\Delta\mathrm{FWHM}/\mathrm{FWHM}_{corr} \lesssim 1\%$.

We combine (A - B) pairs and use IRAF task APALL to extract a 1D spectrum within an interactively-set spatial aperture ($\sim 2''$) in the reduced 2D spectrum. We flux-calibrate the final 1D spectra for our targets using the standard star spectra taken during the same night with the same instrument configurations. We reduce the standard star observations in the same manner as science images. We use the Vega SED (Colina 1996) as a reference and construct a scaled Vega-type spectrum according to the magnitude of the observed standard. We derive flux calibration

corrections at each wavelength by dividing the observed 1D standard spectra by this scaled reference spectrum and apply these calibration corrections to the science 1D spectra. The flux-calibrated 1D spectra for our targets are presented in the bottom panels of Figs. 4.1-4.5.

We characterize the emission features detected in our spectra – Balmer line Hα, and forbidden doublets [NII], [OIII] and [SII] – in terms of integrated line flux, full-width half-maximum and central wavelength of emission. We fit each emission feature with a gaussian curve using the IRAF task SPLOT, allowing the amplitude, width and central wavelengths as free parameters. In the case of several emission features within the same spectra, as is the case for SMM 030227.73 and SMM 123549.44, we fix the relative wavelength offsets between the lines to introduce redshift as a free parameter.

Even after careful flux calibration, significant uncertainties remain in the absolute flux values. The near-IR sky varies on short time scales and so observed standard spectra do not provide an exact correction to the atmospheric absorption when science exposures are taken. Quantification of these uncertainties is difficult. We attempt to estimate these uncertainties by considering the noise in the sky-background during line fitting. For this reason we input the rms of the off-line regions into our fitting routine, to better characterize uncertainties in line integrated flux and FWHM. Furthermore, significant calibration uncertainty is due to slit losses in which the entire target is *not* fully enclosed by the relatively narrow $0.76''$ slit. This may occur either due to: (1) a misalignment of the object within the NIRSPEC slit; (2) considerable seeing $\gtrsim\ 1''$; or (3) as a result that the target is larger than the slit size. In the case of SMGs, the latter is a known source of uncertainty, since the typical extent of Hα emission has been shown to be $\gtrsim\ 4-8$ kpc, which at $z\ \sim\ 2$ corresponds to $0.5-1''$.

4.3.1 Deblending Emission Lines

The Hα lines in our sample are blended with contributions from the [NII] line doublet at $\lambda\ =\ 6549, 6583$ Å. With a line ratio based on transition probabilities of $[\mathrm{NII}]_{6549}$:$[\mathrm{NII}]_{6583}$ equal to 1 : 3 (Osterbrock 1989), we deemed it *reasonable* to decon-

volve the emission complex into two principal emission lines: Hα and NII[6583], using the DEBLENDING mode in the IRAF task SPLOT: we specify the wavelength region for the deblending to be performed, the relative spacing of the lines, and we allow gaussian curves to be fit with redshift, amplitude and FWHM as free parameters.

Similarly, we consider the relative transition probabilities for the forbidden doublets [SII] and [OIII] at $\lambda_{[SII]} = 6716, 6731$ Å and $\lambda_{[OIII]} = 4959, 5007$ Å, with $[\mathrm{SII}]_{6731}$:$[\mathrm{SII}]_{6717} = 3.4$ and $[\mathrm{OIII}]_{5007}$:$[\mathrm{OIII}]_{4959} = 2.86$, respectively (Osterbrock 1989). Since the resolution of our observations does not allow us to discern these two emission features, we consider only the strongest lines during deblending. This results in upper limits for the strengths of $[\mathrm{NII}]_{5007}$ and $[\mathrm{SII}]_{6731}$ if deblending the Hα+[NII] complex is possible and when an [SII] emission feature is detected above the noise level, respectively.

4.4 Results

We present the 2D and 1D near-IR spectra for the SMGs in our study in Figs. 4.1-4.5 and present our results in Table 4.2. The spectra for MIPS J142824.0+352619 is described by Borys et al. (2006). We include it here for completeness.

4.4.1 SMM J030227.73

We detect a prominent emission feature atop a significant continuum for this source (see Fig. 4.1). With an optical redshift of $z_{opt} = 1.408$ (C05), we identify this feature with Hα line emission. There is definite sub-structure within this feature, which we attribute to the blending of the Hα line with the forbidden line doublet [NII]. Furthermore, a faint line is detected at the expected location for the [SII] doublet.

We obtain upper limits for [SII] emission, but our attempt to deblend the Hα+[NII] complex into two distinct components was not successful within reasonable uncertainties. Excluding the contribution from [NII], we extract upper limits to the Hα and [SII] emission for this source. Considering both emission features, we confirm that this source is at $z = 1.407 \pm 0.001$, within 125 km s^{-1} of the optical redshift.

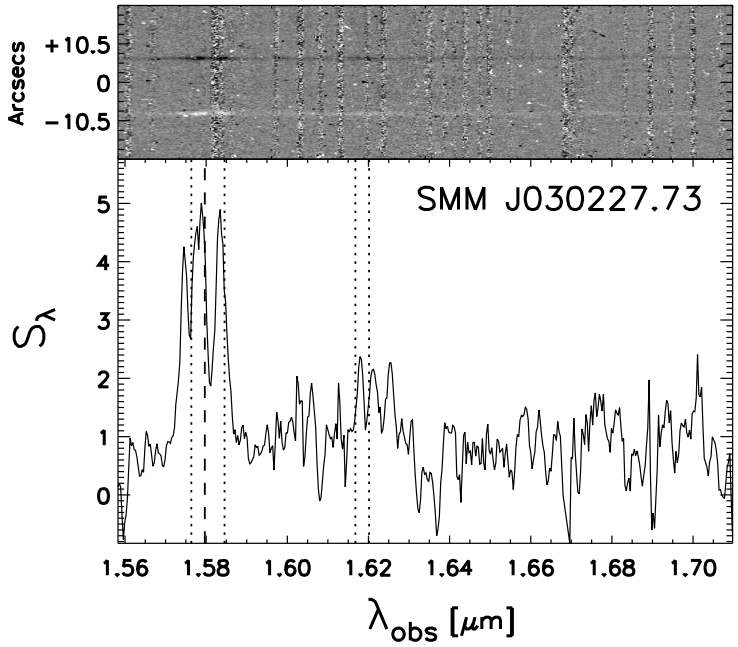

Figure 4.1 Near-IR spectrum of SMM J030227.73. (**Top:**) Fully-reduced, sky-subtracted 2D spectrum with wavelength increasing along the x-axis. Both the positive and negative traces of this object, separated by 10.5″ from the center of the slit, are visible. A broad emission line is evident in both these traces. (**Bottom:**) The flux-calibrated 1D spectrum in the observed frame with flux expressed in units of 10^{-15} erg s^{-1} cm^{-2} μm^{-1}. The central wavelength of the Hα line is indicated by a vertical dashed line and the positions of the [NII] and [SII] doublets are shown by dotted lines. The spectrum is smoothed to 10 Å bins, corresponding to the spectral resolution of the observations.

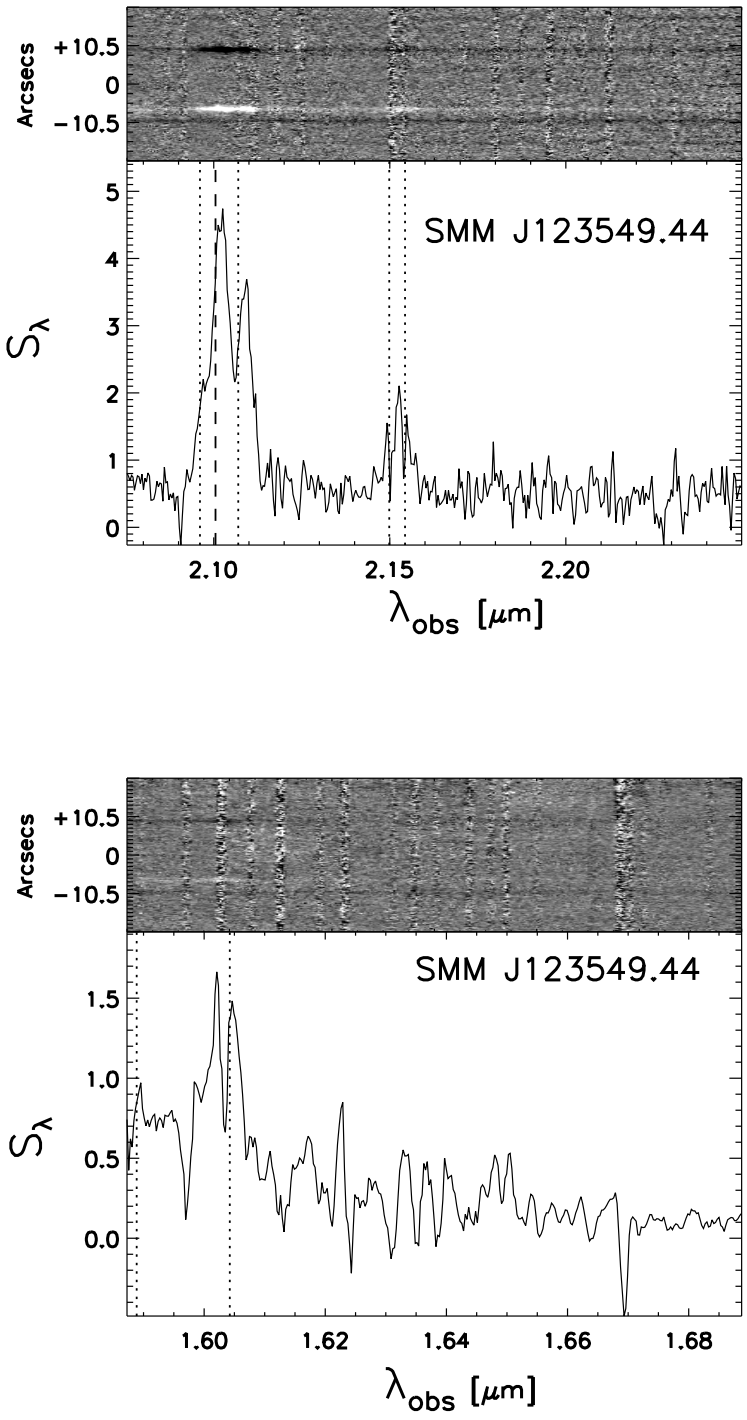

Figure 4.2 Near-IR $K-$ and $H-$band spectra of SMM J123549.44, following the same format as Fig. 4.1.(**Top:**) K-band spectrum of SMM J123549.44 showing clear emission from the Hα+[NII] complex. (**Bottom:**) H-band observations, revealing a fainter, but definite emission from $[OIII]_{5007}$.

4.4.2 SMM J123549.44

This SMG lies within the GOODS-North field and thus benefits from a wealth of multi-wavelength coverage. It has been identified as having AGN signatures in the X-ray (Alexander et al. 2005a), near-IR (S04) and mid-IR (Menéndez-Delmestre et al. 2008) wavebands. Tacconi et al. (2006, 2008) have also undertaken high-resolution CO observations of this galaxy and find CO emission dominated by a compact source ($\lesssim 0.5''$) with a prominent double-peaked CO profile, which they associate with orbital motions of gas within a disk.

H- and the *K*-band follow-up of this SMG reveals clear emission features at the expected locations for Hα, [SII] and [OIII] according the $z_{opt} = 2.2032$ (see Fig. 4.2). The Hα, [SII] and [OIII] emission features for SMM J123549.44 are observed to be broad, with $\sigma_{rest} \sim 800 - 1000$ km s^{-1} (see Table 4.3), which suggests that the observed near-IR emission is associated with AGN activity. Based on the central wavelengths for the observed Hα and [SII] emissions, we constrain the redshift to $z_{H\alpha,[SII]} = 2.205 \pm 0.001$. Considering the location of the [OIII] emission line, we find $z_{[OIII]} = 2.202 \pm 0.001$. The comparison of the rest-frame UV redshift to $z_{H\alpha,[SII]}, z_{[OIII]}$ indicates that there are slight redshift offsets between these lines. Forbidden [OIII] emission is offset from the Hα emission, with $\Delta v \sim 340$ km s^{-1}, while Lyα is at a relative velocity $\Delta v \sim 625$ km s^{-1} with respect to Hα. These differences lie outside the estimated uncertainties $\Delta\lambda \gtrsim 10$ Å, and therefore indicate intrinsic velocity offsets between the emission regions. However, we note that these differences remain quite small in comparison to velocity offsets typically found in quasars, $\Delta v \gg 1000$ km s^{-1}. These velocity offsets fall within the velocity dispersions (FWHM) of the individual emission features, which indicates that the redshift differences are not necessarily the result of systemic velocity differences (which would suggest the presence of outflows), but can be explained in terms of the velocity dispersion within different parts of the galaxy.

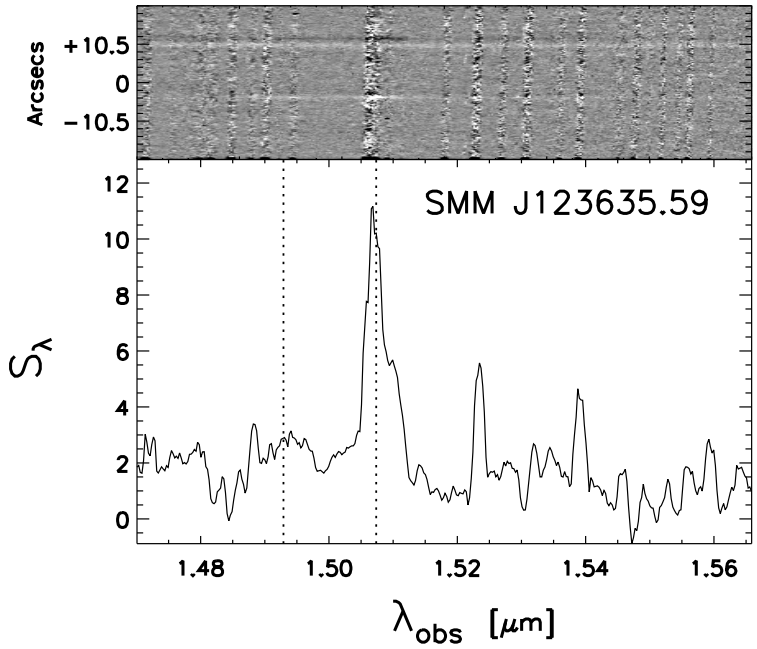

Figure 4.3 Near-IR spectrum of SMM J123635.6, following the same format as Fig. 4.1. We see clear line emission from [OIII] at $\lambda_{rest} = 5007$ Å and at a significantly lower level, a flux excess at the redshifted location expected for $[\mathrm{OIII}]_{4959}$ emission (dotted lines).

4.4.3 SMM J123635.59

This SMG was first identified as an extended μJy radio source and was initially assumed to be powered by star formation (Richards 2000). However, AGN signatures have been reported in the rest-frame UV and optical: Chapman et al. (2005) detect strong CIV ($\lambda_{CIV} = 1550$ Å), which is often associated with quasars. Dawson et al. (2003) and S04 have identified an underlying broad component to the Hα emission (FWHM$_{H\alpha} \gtrsim 2500$ km s^{-1}), and ultra-deep X-ray observations with *Chandra* revealed that this SMG is a source of hard X-ray emission (Alexander et al. 2005a).

To provide more insight, we undertook H-band observations and obtained a clear detection of the forbidden [OIII] emission at $\lambda_{obs} \sim 1.507$ μm. We also have marginal detection of the weaker component of the doublet, [OIII]$_{4959}$, evident as a slight flux excess in the continuum at $\lambda_{obs} \sim 1.493$ μm (see Fig. 4.3). We derive a redshift $z_{[OIII]} = 2.011 \pm 0.001$, which is significantly offset from $z_{opt} = 2.005$ and corresponds to a velocity offset $\Delta v \sim 1640$ km s^{-1}. In contrast to SMM J123549.44, the [OIII] line is relatively narrow ($\sigma_{[OIII]} \sim 330$ km s^{-1}; see Table 4.3), which suggests that this offset is associated with an outflow.

4.4.4 SMM J123716.01

Rest-frame UV observations set this SMG at $z_{opt} = 2.037$. In Fig. 4.4 we show the K-band NIRSPEC spectrum, which clearly shows the Hα+ [NII] emission complex. We make the conservative assumption that the emission complex is dominated by Hα emission and obtain an observed Hα flux of $S_{H\alpha} = 5.0 \times 10^{-15}$ erg s^{-1} cm^{-2}. We compare this value to the Hα flux estimated from Hβ measurements by (Takata et al. 2006), based on the theoretical H$_\alpha$/H$_\beta \sim 2.86$ ratio for an HII-region (Osterbrock 1989). In the case of no extinction, with $S_{H\beta} = 2.81 \pm 0.32 \times 10^{-15}$ erg s^{-1} cm^{-2}, the expected Hα emission corresponds to $S_{H\alpha} \sim 8.0 \times 10^{-15}$ erg s^{-1} cm^{-2}. Therefore, it is clear that the detected Hα emission is being decreased.

This decrease cannot be explained by the contamination from an over-subtracted atmospheric OH line emission. The closest sky line is centered at ~ 2.09 μm, which

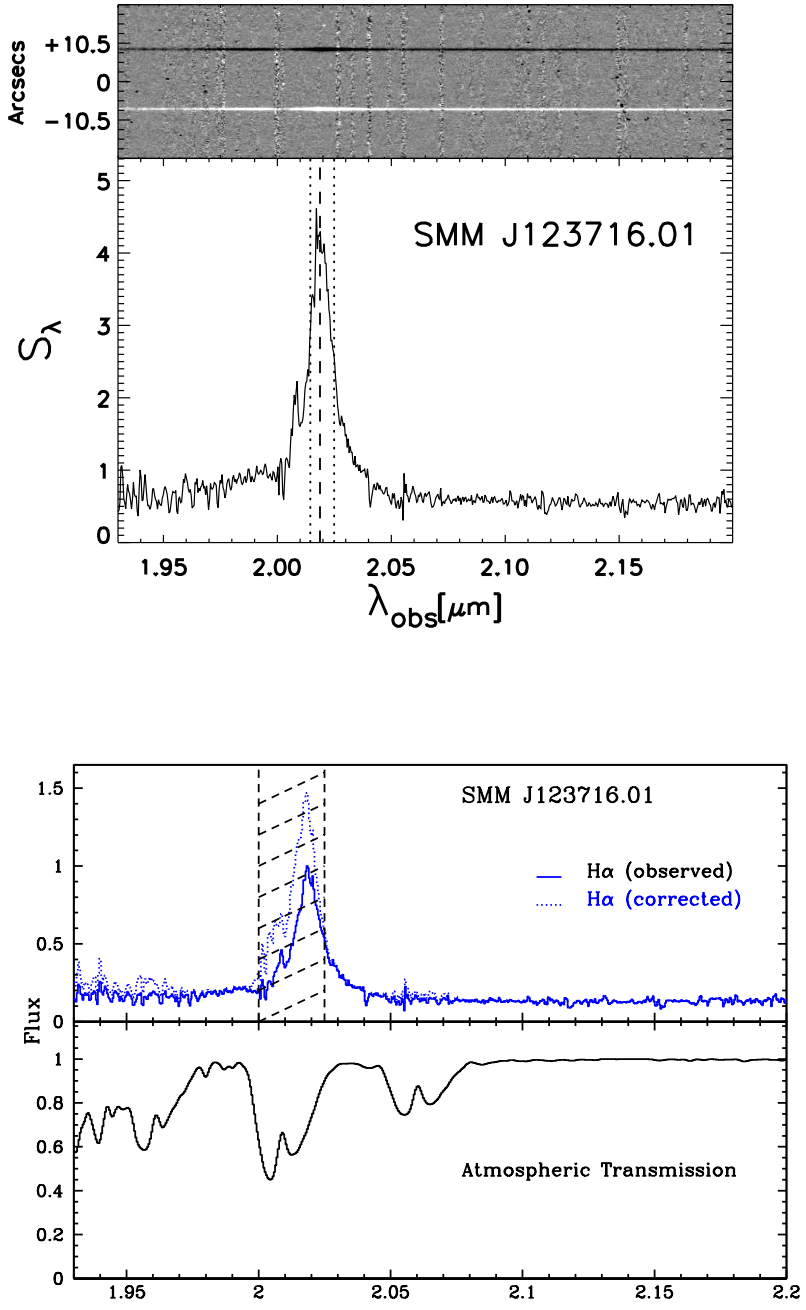

Figure 4.4 (**Top:**) Observed near-IR spectrum of SMM J123716.01, following the same format as Fig. 4.1. (**Bottom:**) Hα emission line spectrum corrected for atmospheric absorption. At this wavelength, atmospheric absorption becomes significant, as the trough in atmospheric transmission in the bottom panel show. To correct for this, we divide our spectrum by the atmospheric transmission to mimic the emission line free of absorption (top panel, dotted-line spectrum). See §4.4.4 for details.

would only affect the red wing of the emission feature. We note that at $z = 2.037$, Hα is redshifted to an observed wavelength range that coincides with a significant trough in the atmospheric transmission (see bottom panel of Fig. 4.4) centered at $\lambda \sim 2.01$ μm. The depth of this trough reduces the atmospheric transmission coefficient by $\sim 40\%$. This results in a measured flux substantially lower than the otherwise unabsorbed Hα+ [NII] emission.

We approximate a correction to this atmospheric absorption by dividing our observed spectrum by the atmospheric transmission and creating an *unabsorbed* version of the spectrum. The *true* emission strength likely lies between these two boundaries. Therefore, we characterize the line emission in both spectra, obtaining line integrated fluxes and FWHMs in both spectra and adopt the average between these two to describe the *unabsorbed* line emission. Considering the complexity presented by this emission feature, we do not attempt to deconvolve the Hα+[NII] complex. We find $z_{H\alpha} = 2.073$ and include these adopted values in Tables 4.2, 4.3.

Note that the resulting absorption-corrected values still lie below the expected value determined from the Hβ in Takata et al. (2006). To explain this mismatch in values, we consider other factors that may be leading to a lower Hα. As discussed in Section 4.3, slit losses may be responsible for a decreased detection of emission from an extended target. We carefully inspected the SCAM images and ensured that the offset star, used for the blind offsets to the science target as described in Section 4.2, was well-centered in the slit. With a seeing of $\simeq 1''$ for these observations, it is likely that SMM J123716.01 was not fully enclosed by the width of the slit. Furthermore, the slit-width of the Subaru OHS spectrograph with which Hβ observations for this object were made is $0.95''$ in comparison to NIRSPEC's $0.76''$. NIRSPEC measurements would amount to 80% of that measured by OHS. This may further explain why our Hα flux corrected for atmospheric absorption still remains below the expected value based on the theoretical Hα/Hβ ratio.

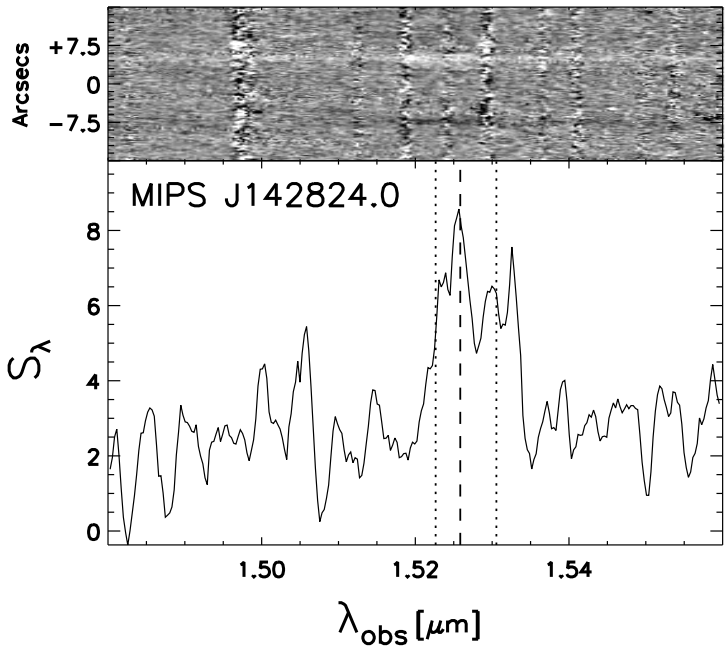

Figure 4.5 Near-IR spectrum of MIPS J142824.0, following the same format as Fig. 4.1. we see that this mm-detected source displays broad Hα emission, blended with flanking [NII] lines at $\lambda = 6459, 6583$ Å.

Table 4.2. Redshifts and Near-IR Integrated Line Fluxes

SMM J	z_{opt}[a]	$z_{H\alpha}$	$z_{[OIII]}$	$z_{[SII]}$	$S_{H\alpha}$[b]	$S_{[NII]}$	$S_{[OIII]}$	$S_{[SII]}$
030227.73	1.4080	1.406	–	2.409	3.054 ± 0.42	1.708 ± 0.42	–	1.341 ± 0.41
123549.44	2.2032	2.203	2.202	2.197	–	–	–	–
123635.59	2.0050	2.015[c]	2.011	–	0.42 ± 0.03[c]	–	0.035 ± 0.002	–
123716.01	2.0370	2.073	–	–	6.60 ± 0.26	–	–	–
MIPS142824.0	–	1.324	–	–	3.01 ± 0.31	2.46 ± 0.35	–	–

[a] From C05

[b] Integrated line flux expressed in unis of 10^{-15} erg s^{-1} cm^{-2}.

[c] From Swinbank et al. (2004).

4.4.5 MIPS J142824.0+352619

This object was first detected in *Spitzer* GTO observations of the NOAO Deep Wide-Field Survey (NDWFS) Boötes field and is discussed in detail by Borys et al. (2006). With strong mid-IR flux and extremely red optical colors ($R-K > 6$), it was inferred that this object was very dust-enshrouded. Follow-up submm observations at 350 μm with the SHARC-II camera (Dowell et al. 2003) on the Caltech Submm Observatory (CSO) and at 850 μm with the SCUBA instrument on the James Clerk Maxwell Telescope (JCMT) provided the shape of the SED of this object. Photometric redshift estimates suggested that this object was at $z > 1$, which suggested that this object was remarkably luminous in the IR, with $L_{8-1000\ \mu m} \gtrsim 10^{13} L_{\odot}$. Devoid of any evident signatures of the presence of an AGN, the large observed IR luminosity suggested that this galaxy was a remarkable specimen that afforded an opportunity to study in detail an example of the relatively unexplored $z = 1 - 2$ dusty starburst population.

Spitzer mid-IR spectroscopy with IRS uncovered strong PAH emission features and placed the galaxy at $z \sim 1.33$ (Desai et al. 2006). However, the intrinsically broad PAH emission features and the relatively low resolution of IRS signified a large uncertainty on this redshift, $\Delta z \sim 0.1$. It is at this stage that a more accurate redshift, based on rest-frame optical emission lines, was necessary.

We show the near-IR spectrum of MIPS J142824.0+352619 in Fig. 4.5. We detect a clear emission feature at $\lambda_{obs} \sim 1.53$ μm, which we identify as Hα emission, likely

blended with the [NII] forbidden line doublet at $\lambda_{rest} = 6549, 6583$ Å. We derive a redshift of $z = 1.323 \pm 0.001$ by fitting gaussians jointly to Hα and the flanking $[\mathrm{NII}]_{6583}$ line. The best fit to this emission indicates a significantly high contribution from [NII] emission, amounting to [NII]/H$\alpha \sim 0.8$. We measure an Hα line width of $\mathrm{FWHM}_{rest} = 1000 \pm 135$ km s^{-1} in the rest-frame, but we caution that this is an upper limit to the intrinsic width, since it may contain contributions from the [NII] lines.

4.5 Discussion

As a result of star formation, the abundance of metals increases in the course of the star-formation history of a galaxy. Rest-frame optical emission line strengths can give us an insight to these chemical abundances. Following the approach of S04, we use the N2-index [1] to estimate the metallicities of the galaxies in our sample. For this, we rely on the calibration by Pettini & Pagel (2004):

$$12 + Log(O/H) = 8.90 + 0.57 \times N2. \tag{4.1}$$

We find that the galaxies in our sample have N2-indices that place them close to solar metallicity (see Table 4.4), within the range found by S04. These results together with other studies on the metal abundance hosted by SMGs (e.g., Tecza et al. 2004) show that SMGs are metal-rich galaxies, with $Z/Z_{\odot} \gtrsim 1$ (see also Bouché et al. 2007).

SMGs have been found to display large redshift offsets between Lyα, Hα and molecular CO lines of up to $few \sim 1000$ km s^{-1} (Smail et al. 2003, 2004; Greve et al. 2005). These redshift offsets indicate that large velocity outflows are sometimes found in these objects. In Fig. 4.6 we compare near-IR redshifts to optical redshifts presented by C05, including those available for four SMGs in our sample. We find that two SMGs in our sample have Hα and optical redshifts within $\Delta z \lesssim 10$ Å of each other,

[1] $N2 = Log([NII]/H\alpha)$

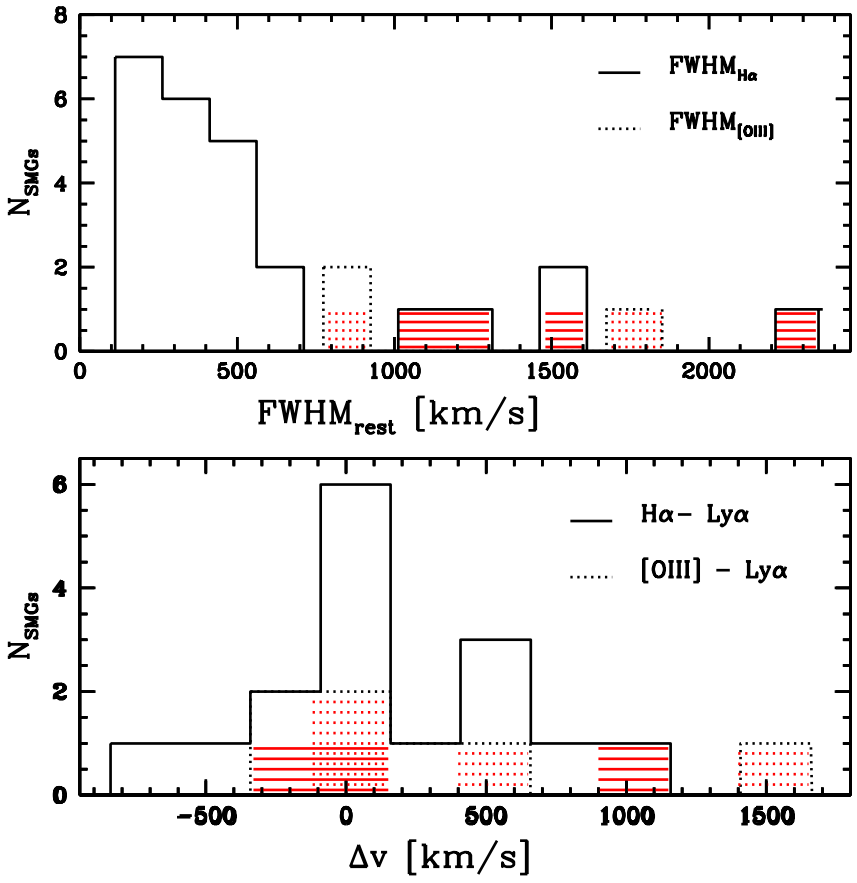

Figure 4.6 (**Bottom:**) Distribution of relative velocities in SMGs as given by differences in rest-frame UV redshifts from C05 and rest-frame optical redshifts, derived from Hα (solid histogram) and [OIII] (dotted histogram) observations. We include objects from S04 and Takata et al. (2006) in addition to the objects in our sample. The hatched regions distinguish the contribution from our sample to these histograms: Hα and [OIII] offsets from Lyα are shown by solid- and dotted-hatched regions, respectively. The velocity offset we find for the QSO-classified SMG SMM J123716.01 falls outside of the displayed region (see § 4.4 for details). (**Top:**) Following the same line-coding as the bottom figure, distribution of line widths (FWHM$_{rest}$) for SMGs.

which corresponds to our spectral resolution. In the cases of SMM J123635.59 and SMM J123716.01, we find $\Delta z = 0.01, 0.036$, respectively. These redshift differences translate into relative velocities of ~ 1000 km s^{-1} for SMM J123635.59 and ~ 3500 km s^{-1} for SMM J123716.01.[2] The SMG SMM J123716.01 has been identified as a QSO by C05, which explains the very large velocity outflow (see also Takata et al. 2006).

Strong outflows have also been identified in extreme objects, such as QSOs (Richards et al. 2002: $\gg$ *few* $\times$ 1000 km s^{-1}) and in populations of less-massive, high-redshift galaxies: optically-selected LBGs display velocity offsets ~ 750 km s^{-1} (Adelberger et al. 2003). Detection of CIV and OIV absorption near QSOs and LBGs (e.g., Adelberger et al. 2003) signals the effect that such ionizing outflows may have in enriching their surroundings. Given that SMGs are among the most luminous objects in the universe, it is to be expected that SMGs host stronger outflows than LBGs. Considering the chemical abundances of SMGs, such outflows are potentially powerful at transforming the intergalactic environments rapidly.

4.5.1 AGN Signatures in SMGs

The near-IR provides with a number of diagnostic lines that can be used to probe for the presence of an underlying AGN. Veilleux et al. (1995) explored the use of the [SII]/Hα ratio to classify galaxies into different spectral types. They analyzed a large sample of 200 bright IRAS sources and classified them into spectral types according to a number of intensity ratios, including [SII]/Hα and [NII]/Hα. Two sources in our sample – SMM J123549.44 and SMM J030227.73 – display [SII] emission, with [SII]/H$\alpha \sim 0.2, 0.4$, respectively (see Table 4.3). According to Veilleux et al. (1995), these ratios are clear AGN signatures commonly found in low-ionization nuclear emission-line regions (LINERs) and Seyfert galaxies.

The presence of an AGN can also be probed through detection of broad emission lines. Broad line emission may be associated with ordered orbital motions of gas but

[2] $\Delta \mathrm{v} = |\mathrm{z_{opt}} - \mathrm{z_{H\alpha}}|/(1 + \mathrm{z_{opt}})$

Table 4.3. Summary of Spectral Classifications

SMM J	FWHM$_{H\alpha}$[a] km s^{-1}	FWHM$_{[OIII]}$[a] km s^{-1}	[NII]/Hα	[SII]/Hα	Class	Comments
030227.73	1500 ± 266	–	0.56 ± 0.21	0.44 ± 0.19	SB;[b] AGN[c]	high [SII]/Hα-ratio; FWHM$_{H\alpha}$ > 500 km s^{-1}
123549.44	1183 ± 43	1850 ± 37	0.56 ± 0.04	0.19 ± 0.02	SB;[b] int	FWHM$_{H\alpha}$ > 500 km s^{-1}
123635.59 (nw)[d]	240 ± 33	775 ± 40	0.67 ± 0.27[e]	–	AGN[e]	[NII]/Hα > 0.7; Broad Hα, [OIII]
123635.59 (br)	1623 ± 213[e]	775 ± 40				
123716.01	2349 ± 94	–	–	–	QSO[b]AGN[f]	FWHM$_{H\alpha}$ > 500 km s^{-1}
MIPS142824.0	1042 ± 135	–	0.82 ± 0.20	–	SB [g]AGN	[NII]/Hα > 0.7; FWHM$_{H\alpha}$ > 500 km s^{-1}

[a] FWHM are expressed in rest-frame and derived assuming $z = z_{H\alpha}$.

[b] From rest-frame UV (C05).

[c] From Hα integral field spectroscopy Swinbank et al. (2006).

[d] Dawson et al. (2003) and Swinbank et al. (2004) distinguish a narrow and broad Hα component for this SMG.

[e] From long-slit Hα spectroscopy (Swinbank et al. 2004).

[f] From long-slit Hα spectroscopy (Takata et al. 2006).

[g] From Borys et al. (2006).

it can also be the result of having a direct view of the randomly moving high-velocity gas within the broad-line region of a central AGN. S04 have shown that 40% of SMGs display a broad Hα component, with FWHM$_{rest}$ $\sim$ 500 $-$ 3000 km s^{-1}. These line-widths are narrower than those typically found for classical quasars (FWHM$_{H\alpha}$ $\gtrsim$ 2$-$ 8 $\times$ 10^3 km s^{-1}; e.g., Puchnarewicz et al. 1997), but are markedly larger than those found for other populations of starburst-dominated galaxies (e.g., FWHM$_{rest}$ $\lesssim$ 500 km s^{-1} in LBGs; Erb et al. 2003). In Fig. 4.6 we see that the galaxies in our sample display among the broadest Hα and [OIII] line-widths that have been identifed in SMGs. These large velocity dispersions suggest that we are seeing the broad-line region close to a central AGN.

S04 separate SMGs into three classes (see Fig. 4.7): an AGN-dominated class with FWHM$_{H\alpha}$ $\gtrsim$ 1000 km s^{-1} and/or [NII]/Hα $>$ 0.7; a class of composite systems displaying intermediate line-widths, FWHM$_{H\alpha}$ $\sim$ 500 $-$ 1000 km s^{-1}; and a class of SMGs with no evident AGN signatures, likely dominated by star formation (FWHM$_{H\alpha}$ $\lesssim$ 500 km s^{-1} and [NII]/Hα $<$ 0.7). All the galaxies in our sample display line-widths or [NII]/Hα line ratios that place them in either the AGN- or composite-class (see Fig.4.7 and Table 4.3).

Three out of five of our targets include ultra-deep *Chandra* X-ray data and have been identified as hard X-ray sources (Alexander et al. 2005a). We have included these X-ray classifications as well as the classifications based on other observed wavelengths in Table 4.3. Our near-IR classification based on line-widths and line ratio diagnostics is in agreement with AGN signatures at other wavelengths. The only exception is MIPS 142428.04. Uncertainties in the deblending of the Hα+[NII] complex remains an important caveat to these results and are a potential source of disagreement. The combination of broad Hα and high [NII]/Hα line ratio strongly suggests that this object harbors an AGN. However, the contribution of the AGN to the total luminous output of this galaxy does not necessarily dominate over the the contribution from star-forming activity (Borys et al. 2006).

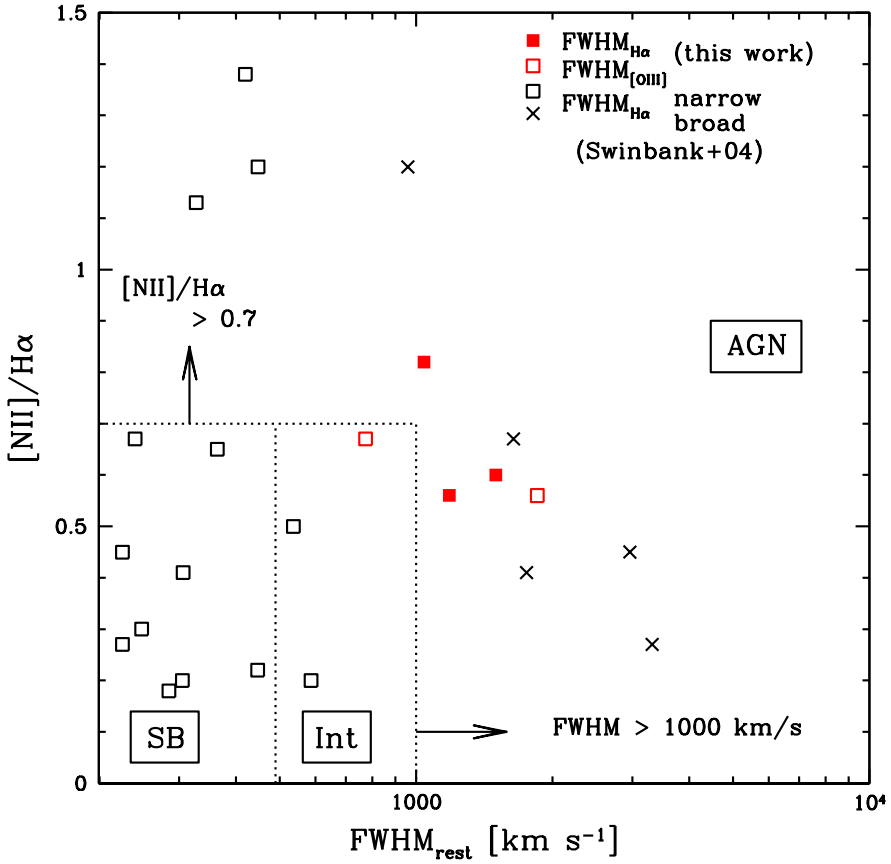

Figure 4.7 [NII]/Hα line ratios as a function of Hα and [OIII] line widths for SMGs, with the objects presented in this work highlighted. We include results from the near-IR spectroscopic program presented by S04 and include their classification into starburst (SB), AGN-dominated (AGN) and AGN+SB composites (Int). See §4.5.1 for details.

4.5.2 Star Formation Rates

Submm- and mm- selected galaxies are dusty systems and thus suffer from significant extinction. In the near-IR, the obscuration is not as high as in the optical, but still remains an important caveat to the observed line luminosities. Takata et al. (2006) show that the Hα-derived SFRs for these objects, with no correction for reddening are systematically lower than those derived from the total infrared luminosity $L_{8-1000\ \mu m}$ (Takata et al. 2006).

Takata et al. (2006) have shown that SMGs typically have observed Hα/Hβ $\sim$ 5$-$20, corresponding to extinction levels in the range $A_v \sim 1-4$ with a median $< A_v >= 2.9 \pm 0.5$, using the reddening curve from Calzetti et al. (2000).[3] Line emission from Hβ falls at 4861 Å, bluewards of $\lambda_{H\alpha} = 6563$ Å and it thus suffers more from dust obscuration than Hα. The intrinsic, unobscured ratio between these recombination Balmer lines is expected to be 2.86 (Osterbrock 1989). Therefore, comparison of the observed Hα/Hβ ratio with the intrinsic value, called the *Balmer decrement*, provides with an estimate of the extinction along the line of sight:

$$S_{H\alpha}(\tau_\lambda \sim \tau_{\rm Balmer}) = S_{H\alpha}(\tau_\lambda = 0) \times e^{-\tau_{\rm Balmer}} \tag{4.2}$$

$$\tau_{\rm Balmer} = \tau_\beta - \tau_\alpha = \ln[\frac{\rm H\alpha/H\beta}{2.86}]. \tag{4.3}$$

We apply a reddening correction of $e^{\tau_{Balmer}} \sim 4$ to the measured Hα luminosities assuming a *typical* Balmer decrement ~ 10 (see Table 4.4). This factor is significantly larger than the typical attenuation found for other high-redshift populations, such as the optically-selected LBGs, with attenuations of an average factor of 1.7 (Erb et al. 2006a). This demonstrates that an increased level of internal extinction is found in SMGs, with respect to other well-studied high-redshift populations.

We estimate SFRs in our targets from the reddening-corrected Hα line, assuming the following relation presented by Kennicutt (1998):

[3] Assuming the simplified case of a dust screen in the line of sight to the source, $E(B-V) = 0.935 \times [\ln(\rm H\alpha/H\beta) - \ln(2.86)]$ (Calzetti et al. 1994).

Table 4.4. Star Formation Rates, Metallicities and Dynamical Masses

SMM J	$L_{H\alpha}$[a] L$\odot$	$L_{8-1000\mu m}$[b] 10^{12} L$\odot$	$SFR_{H\alpha}$ $M_\odot$ s^{-1}	SFR_{IR} $M_\odot$ s^{-1}	M_{dyn} $M_\odot$	$12 + Log(O/H)$[c]
SMMJ030227.73	9.85×10^{10}	27.80	2978	4788	3.77×10^{12}	8.76
SMMJ123635.59	3.31×10^{10}	4.05	1001	697	9.68×10^{10}	–
SMMJ123549.44	–	4.45	–	766	2.35×10^{12}	8.76
SMMJ123716.01	5.58×10^{11}	5.25	–	904	–	–
MIPS142824.0	8.35×10^{10}	16.00	2526	2755	1.82×10^{12}	8.85

[a] Extinction-corrected using typical Balmer decrement found for SMGs by Takata et al. (2006). See §4.5.2 for details.

[b] We use total infrared luminosities from C05, corrected by approximately a factor of two, following Kovács et al. (2006)

[c] Derived from N2-index. See §4.5 for details.

$$SFR\,[\mathrm{M_\odot\,yr^{-1}}] = 7.9 \times 10^{-42} \times (L_{H\alpha}[\mathrm{erg\,s^{-1}}]). \tag{4.4}$$

With observed Hα luminosities (not corrected for extinction) in the range of $0.3 - 6 \times 10^{11}$ L$_\odot$, and assuming that the Hα line characteristics are due to star formation, the targets in our sample have SFRs $\sim 400 - 1200$ M$_\odot$ yr^{-1}. The SMG SMM J123716 has been previously identified as a QSO and thus the particularly wide Hα line (and consequently, very large Hα luminosity) is clearly a reflection of the ionization and kinematics within the AGN's broad line region.

We compare SFRs calculated from the existing Hα measurements and those derived from the total IR emission (Kennicutt 1998). For the latter we use $L_{8-1000\ \mu m}$ by C05, which are estimated from radio and submm-wave flux densities, corrected by approximately a factor of two, following Kovács et al. (2006). We find that even when corrected for extinction (as shown in Table 4.4), Hα-derived SFR estimates still remain a factor of $2 - 4$ less than those derived from the IR luminosity. These results are in reasonable agreement with the analysis of Takata et al. (2006). This suggests that additional extinction, unaccounted for by the Balmer decrement, may be present.

4.5.3 Stellar Dynamical Masses

From the widths of the rest-frame optical emission lines we can obtain estimates of dynamical masses for the galaxies in our sample. The relation between line-width and dynamical mass relies on the assumption that line-broadening is due to the motion of the gas in the general, large-scale gravitational potential well of the galaxy. For the sake of simplification, we approximate a galaxy to a sphere of uniformly distributed gas. For this case, the dynamical mass is given by:

$$M_{dyn} = 5 \times \sigma^2_{rest}(R/G), \tag{4.5}$$

where σ = FWHM/2.355 is the velocity dispersion of the gas, R is the radial size of the gas distribution and G is the gravitational constant. Hα narrow-band emission observations have shown that SMGs have a typical (seeing-corrected) radial size of 0.5–1$''$ or 4–8 kpc (Smail et al. 2004), while integral field spectroscopic observations have shown that the Hα distribution may extend out to $\sim 2''$ or 16 kpc (Swinbank et al. 2006). Assuming an Hα spatial extension of 1$''$, Hα line-widths in our study result in dynamical masses in the range of $M_{dyn} \sim 10^{11} - few \times 10^{12}$, with a median value of $< M_{dyn} >= 2.4 \pm 3.2 \times 10^{12}$ M$_\odot$ (see Table 4.4).

SMG masses are expected to be significant in order to retain a substantial amount of processed metal-rich gas in the interstellar medium, as observed in isolated cases (Tecza et al. 2004). However, we note that important caveats must be kept in mind in deriving stellar dynamical masses. Long-slit spectroscopy only provides us with an insight to the integrated emission of the galaxy. Therefore, it is very challenging to distinguish between the fraction of a broad Hα line due to ordered gas motions reflecting the dynamics of the entire galaxy and Hα emission arising from the broad line region of a central, albeit possibly weak, AGN. S04 have attempted to disentangle the broad and narrow-Hα components and have derived a median stellar dynamical mass $< M_{dyn} >\sim (1.5 \pm 0.9) \times 10^{11}$ M$_\odot$.

Greve et al. (2005) report median dynamical masses $< M_{dyn} >\sim 1.2\pm1.5\times10^{11}$ M$_\odot$ from detailed mapping of CO emission of 12 CO-detected SMGs. These observations

target higher CO transitions ($J \geq 2$) and thus trace mainly the dense, warm molecular gas in these galaxies definitely not associated with an AGN. It is thus possible that larger dynamical masses are traced by the colder, more extended molecular medium. Stellar masses of $\sim 10^{11}$ $M_\odot$ have been inferred from SED fitting of near-IR and optical aperture photometry (Borys et al. 2005). However, recent work by Maraston et al. (2006) suggests that popular stellar population models do not include a proper treatment of thermally pulsing asymptotic giant branch (TP-AGB) stars, which can result in significantly lower photometric mass estimates for high redshift galaxies, where TP-AGB stars are expected to contribute strongly to the galaxy SED.

The collection of these results indicates that reliable mass estimates for SMGs are still a work in progress. However, studies agree that SMGs are massive galaxies. The presence of such large masses already in place at these high redshifts, together with the large number density of these objects poses strong constraints in current theories of mass assembly. In order to reconcile these stellar masses and SFRs at $z \sim 2$ with the masses of local massive ellipticals, Baugh et al. (2005) have suggested that a top-heavy initial mass function may be at work in these galaxies. However, the appeal to a flat IMF and the validity of this assumption remains controversial. Both theoretical work and observational constraints remain necessary to develop a model of galaxy formation to reproduce the observed galaxy counts in the low- and high-redshift universe.

4.6 Conclusions

We present near-IR observations of five mm- and submm- detected galaxies in continuation of a large program to investigate the rest-frame optical emission of high-redshift ULIRGs. We derive dynamical masses and star-formation rates for these objects: $M_{dyn} \sim 10^{12}$ $M_\odot$ and $SFR \sim 1 - 3 \times 10^3$ $M_\odot$ yr^{-1}, assuming a typical extinction in the near-IR corresponding to a Balmer decrement Hα/H$\beta \sim 10$. These results provide further evidence supporting that mm- and submm-selected ULIRGs at high-redshift are highly massive systems undergoing intense star-forming activity.

We also find large velocity offsets between rest-frame UV and Hα lines for two of our objects, suggesting that strong outflows are present. With near- to super-solar metallicities, SMGs are likely rapidly enriching their environments.

Our observations also show clear AGN-like broad line signatures and/or high [NII]/Hα spectral diagnostic ratios in all five of our targets. We emphasize that when both star formation and an AGN are present, even though the high S/N of our low-resolution NIRSPEC observations is sufficient to detect clear AGN signatures, long-slit spectroscopic techniques face difficulties in disentangling their independent contributions and may result in overestimates of the SFRs and stellar masses of SMGs. This motivates greatly the pursuit of exploring the two-dimensional spatial distribution of line emission that recent integral field spectrographs provide. We have initiated such an effort with the OH-Suppressing Infrared Spectrograph (OSIRIS; Larkin et al. 2006) on Keck, as we discuss in Chapter 5.

Acknowledgements We thank the team of support astronomers, telescope operators and the staff members at the Keck Observatories for their assistance with the observations. In particular, we thank Jim Lyke, Grant Hill and Al Conrad for their excellent on-site support. We are also grateful to Dawn Erb for insightful discussions and her guidance in the reduction of NIRSPEC data. The data presented herein were obtained at the W.M. Keck Observatory, which is operated as a scientific partnership among the California Institute of Technology, the University of California and the National Aeronautics and Space Administration. The Observatory was made possible by the generous financial support of the W.M. Keck Foundation. The authors wish to recognize and acknowledge the very significant cultural role and reverence that the summit of Mauna Kea has always had within the indigenous Hawaiian community. We are most fortunate to have the opportunity to conduct observations from this mountain.